



Electron microscopy analysis of Ti-substituted Li_2MnO_3 positive electrode before and after carbothermal reduction

T. Akita*, M. Tabuchi, Y. Nabeshima, K. Tatsumi, M. Kohyama

Research Institute for Ubiquitous Energy Devices, National Institute of Advanced Industrial Science and Technology (AIST), Midorigaoka 1-8-31, Ikeda, Osaka 563-8577, Japan



HIGHLIGHTS

- Ti-substituted Li_2MnO_3 before and after reduction was characterized.
- The transition metal distribution was clarified by STEM–EELS in Ti-substituted Li_2MnO_3 .
- The valence state of Ti and Mn was clarified by EELS with high energy resolution.
- Spatial distribution of valence state of Mn was visualized by STEM-EELS method.

ARTICLE INFO

Article history:

Received 19 September 2013

Received in revised form

29 November 2013

Accepted 19 December 2013

Available online 27 December 2013

Keywords:

Li ion battery

Ti-substituted Li_2MnO_3

Electron energy loss spectroscopy

Spectrum imaging

ABSTRACT

40%-titanium substituted Li_2MnO_3 ($\text{Li}_{1+x}(\text{Ti}_{0.4}\text{Mn}_{0.6})_{1-x}\text{O}_2$, $0 < x < 1/3$) before and after carbothermal reduction was characterized by annular dark field scanning transmission electron microscopy (ADF-STEM) and electron energy-loss spectroscopy (EELS) to investigate the effects of the pre-reduction treatment. EELS spectra with high energy resolution using monochromator clearly reveal the appearance of reduced Mn ions after the reduction process. The spatial distribution of the reduced phase was visualized by multi-linear least-squares (MLLS) fitting method using Mn L -edge energy-loss near-edge structure (ELNES). The morphology change of a primary particle was observed around the Mn reduction phase.

© 2014 Elsevier B.V. All rights reserved.

1. Introduction

Rechargeable lithium-ion batteries are key components of portable electronic equipments, electric vehicles, energy storage devices for renewable energy, etc. The high energy and power densities have been indispensable for applications for such devices. As a new high energy density positive electrode materials, it has been reported that the Li-rich solid-solution layered positive electrode materials denoted as Li_2MnO_3 – LiMO_2 ($M = \text{Cr}, \text{Mn}, \text{Fe}, \text{Co}, \text{Ni}$) [1,2] exhibit capacity higher than 250 mAh g^{-1} at 2.0 – 4.8 V region [2–5]. Among transition-metal elements, Fe or Ti is attractive because they are abundant and inexpensive resources [5,6]. The mechanism of such high performance of this kind of positive electrode materials has not yet been clarified.

Recently, it has been reported that Ti-substituted Li_2MnO_3 also exhibit high capacity, and especially, pre-reduction treatment (carbothermal reduction) improves the initial cycle efficiency and cycle performance [6]. At present, the performance of Ti-substituted Li_2MnO_3 as cathode electrode is not necessarily superior to Fe-substituted Li_2MnO_3 for example, while we deal with Ti-substituted Li_2MnO_3 in this work because of their interesting electrochemical performance; reduced Mn ions by the pre-reduction can be re-oxidized to tetravalent state above 3.5 V on initial charging, which was more clearly seen than Fe-substituted one in our previous study [6]. In addition, Ti-substituted Li_2MnO_3 is of much importance in the viewpoint of material design of Li_2MnO_3 -based positive electrode material. Conventionally, cations with valence states less than $3+$ like Cr, Fe, Co and Ni are added as active elements as LiMO_2 component in Li_2MnO_3 – LiMO_2 . In the case of Ti-substituted Li_2MnO_3 , reduced Mn ions play the same role as the active elements, and Ti ions seem to act as simple constituent element of Li_2MO_3 or to be effective in avoiding the formation of impurity phases like LiMnO_2 or MnO [6].

* Corresponding author. Tel.: +81 72 751 9754; fax: +81 72 751 9714.

E-mail address: t-akita@aist.go.jp (T. Akita).

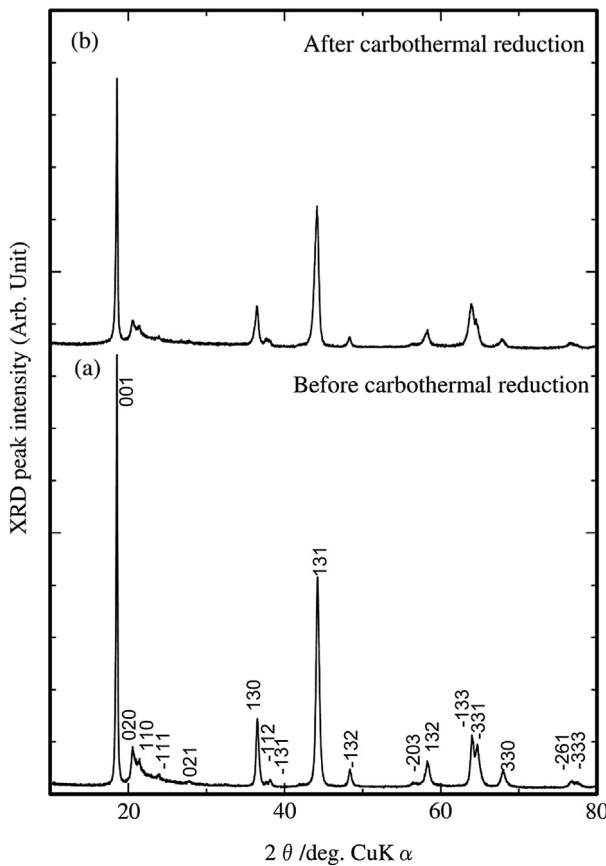


Fig. 1. XRD pattern of $\text{Li}_{1+x}(\text{Ti}_{0.4}\text{Mn}_{0.6})_{1-x}\text{O}_2$ samples before (a) and after (b) the carbothermal reduction.

Understanding of the role of the pre-reduction process is an important clue to clarify the electrochemical activation phenomena of Li-rich solid-solution layered positive electrode materials. Characterization of fine structure in nano and atomic scale is significant to study the activation mechanism during the charge and discharge run of the Li_2MnO_3 – LiMO_2 positive electrode materials. Analytical transmission electron microscopy (TEM) method is one of the most powerful techniques to investigate the morphology, compositions and electronic structure of each particle or each local region of electrode materials. Especially, electron energy-loss spectroscopy (EELS) is suitable for estimation of valence-state distribution of constituent transition-metal atoms in positive electrode materials.

In this report, we focused on the fine structure characterization of 40% Ti-substituted Li_2MnO_3 positive electrode material ($\text{Li}_{1+x}(\text{Ti}_{0.4}\text{Mn}_{0.6})_{1-x}\text{O}_2$, $0 < x < 1/3$) before and after the carbothermal reduction, by using aberration-corrected analytical TEM. We applied the high energy resolution EELS by monochromator for the estimation of valence-state distribution of constituent transition-

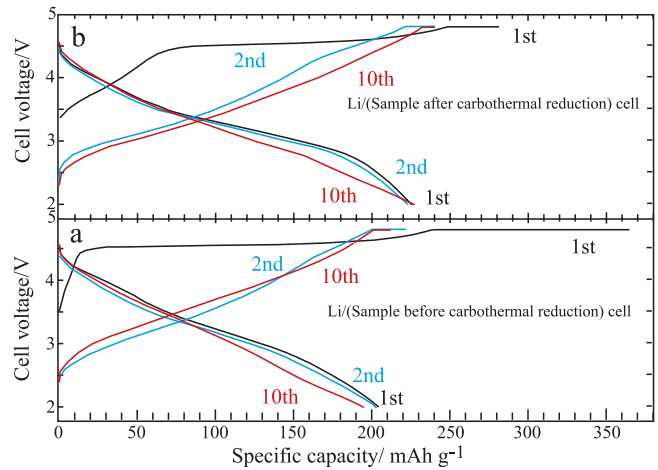


Fig. 2. Initial, second, and 10th charge and discharge curves at 30 °C for $\text{Li}/\text{Li}_{1+x}(-\text{Ti}_{0.4}\text{Mn}_{0.6})_{1-x}\text{O}_2$ cells using samples before (a) and after (b) the carbothermal reduction.

metal ions in the positive electrode materials after the carbothermal reduction.

2. Experimental

Experimental samples were synthesized using four-step processes comprising co-precipitation, hydrothermal reaction, calcination in air, and carbothermal reduction in an N_2 atmosphere. The final transition metal ratio can be adjusted by nominal mixing one of iron (III) nitrate ($\text{Fe}(\text{NO}_3)_3 \cdot 9\text{H}_2\text{O}$, Wako Pure Chemical) and titanium (IV) sulfate (30% $\text{Ti}(\text{SO}_4)_2$ soln., Wako Pure Chemical). The obtained sample was reduced by the carbothermal process using sucrose in order to improve the initial cycle efficiency and cycle performance. The details about the preparation and carbothermal reduction process are described in our previous report [6]. The sample quality was checked using X-ray diffraction (XRD) measurements. The XRD data were obtained by an X-ray diffractometer (Rotaflex RU-200B/RINT; Rigaku). Computer program (RIETAN-2000 [7]) was used for X-ray Rietveld analysis.

The samples before and after the carbothermal reduction was observed by analytical TEM (JEOL JEM-3000F) and aberration-corrected analytical TEM (FEI, Titan³ G2 60–300) equipped with monochromator and Gatan Quantum EELS spectrometer. The powder samples were directly dispersed on the holey carbon micro-grid on Cu mesh without solvent. The Cu mesh was set in the double tilt specimen holder. High-resolution annular dark field scanning transmission electron microscopy (ADF-STEM) images are obtained with the collection angle range of 56–298 mrad. The STEM-EELS spectrum imaging data set was obtained by the 0.1–0.2 s pixel⁻¹. The full width at half maximum (FWHM) of the zero loss peak was approximately 0.2 eV for short acquisition time. Noise in spectra was reduced from the data set of spectrum imaging by principal component analysis (PCA) program (HREM Research

Table 1

X-ray diffraction Rietveld refinement results for Ti-substituted Li_2MnO_3 before and after carbothermal reduction.

Sample	$a/\text{\AA}^2$	$b/\text{\AA}^2$	$c/\text{\AA}^2$	$\beta/^\circ$	$V/\text{\AA}^3$
1. $\text{Li}_{1+x}(\text{Ti}_{0.4}\text{Mn}_{0.6})_{1-x}\text{O}_2$ before reduction	5.0006(14)	8.6277(16)	5.0580(9)	109.292(21)	205.965(79)
2. $\text{Li}_{1+x}(\text{Ti}_{0.4}\text{Mn}_{0.6})_{1-x}\text{O}_2$ after reduction	5.0041(14)	8.6143(17)	5.0512(11)	109.262(25)	205.555(84)

$M = \text{Ti, Mn}$, Unit cell: monoclinic $C2/m$.

Sample 1: Reliability factors, $R_{wp} = 17.80$, goodness of fit indicator, $S = 2.355$.

Sample 2: Reliability factors, $R_{wp} = 13.21$, goodness of fit indicator, $S = 1.735$.

Inc.) on Gatan Digital micrograph software. The distribution of quasi valence state of Mn was obtained by multi-linear least-squares (MLLS) fitting method [8].

3. Results and discussion

3.1. Morphology and atomic structure

Fig. 1 shows X-ray diffraction (XRD) pattern of $\text{Li}_{1+x}(\text{Ti}_{0.4}\text{Mn}_{0.6})_{1-x}\text{O}_2$ samples ($0 < x < 1/3$) before and after the carbo-thermal reduction. All the diffraction peaks belong to monoclinic Li_2MnO_3 -type ($C2/m$) structure. Although the peak positions are almost the same, each peak is broadened after the reduction. The results of Rietveld refinement are shown in Table 1. The Rietveld analyses clarified the substitutional occupancy of Li (2b site) by transition metal atoms, which was slightly increasing after the reduction. This result indicates a certain degree of randomness of the Li and transition-metal atoms in the crystal, which is induced by the reduction. The average transition metal occupancy per chemical formula also increased after reduction. Namely, oxygen atoms were desorbed to some extent after reduction process. The following results were obtained from the chemical analysis. While the ratio of Ti and Mn is maintained after the reduction, the quantity of Li atoms compared to that of transition-metal atoms in the crystal is decreased from 1.98 to 1.48. Nominal compositions were $\text{Li}_{1+x}(\text{Ti}_{0.4}\text{Mn}_{0.6})_{1-x}\text{O}_2$ ($x = 0.329$)

and $\text{Li}_{1+x}(\text{Ti}_{0.4}\text{Mn}_{0.6})_{1-x}\text{O}_2$ ($x = 0.194$) before and after the reduction, respectively, which can be also expressed as $0.987\text{Li}[\text{Li}_{1/3}\text{M}_{2/3}]\text{O}_2 - 0.013\text{LiMO}_2$ and $0.582\text{Li}[\text{Li}_{1/3}\text{M}_{2/3}]\text{O}_2 - 0.418\text{LiMO}_2$ ($M = \text{Ti, Mn}$), respectively. Thus the mean value of oxidation state of Mn is decreased.

Fig. 2 shows the initial, second, and 10th charge and discharge curves for $\text{Li}_{1+x}(\text{Ti}_{0.4}\text{Mn}_{0.6})_{1-x}\text{O}_2$ samples before and after the reduction. Detailed charge and discharge conditions for the electrochemical measurements were described in our previous report [6]. By the reduction, the initial charge capacity decreases from 365 to 281 mAh g^{-1} , while the initial discharge capacity increases from 205 to 225 mAh g^{-1} , indicating the better initial cycle efficiency. The decrease of Li_2MO_3 component and the increase of LiMO_2 after the reduction should be responsible for the decrease of the initial charge capacity. This decrease should be also explained first by the decreased Li quantity in the electrode by the reduction, and second by the decreased contribution of oxygen in charging process by the reduction treatment. The cycle performance until 10th cycle was improved by the reduction. The initial charge capacity below 4.5 V was also improved from 10 to 50 mAh g^{-1} . This feature suggests that Mn^{3+} ions formed by the carbothermal reduction can participate in the initial charge reaction below 4.5 V.

Typical low-magnification TEM images of the samples before and after the carbothermal reduction are presented in Fig. 3. The

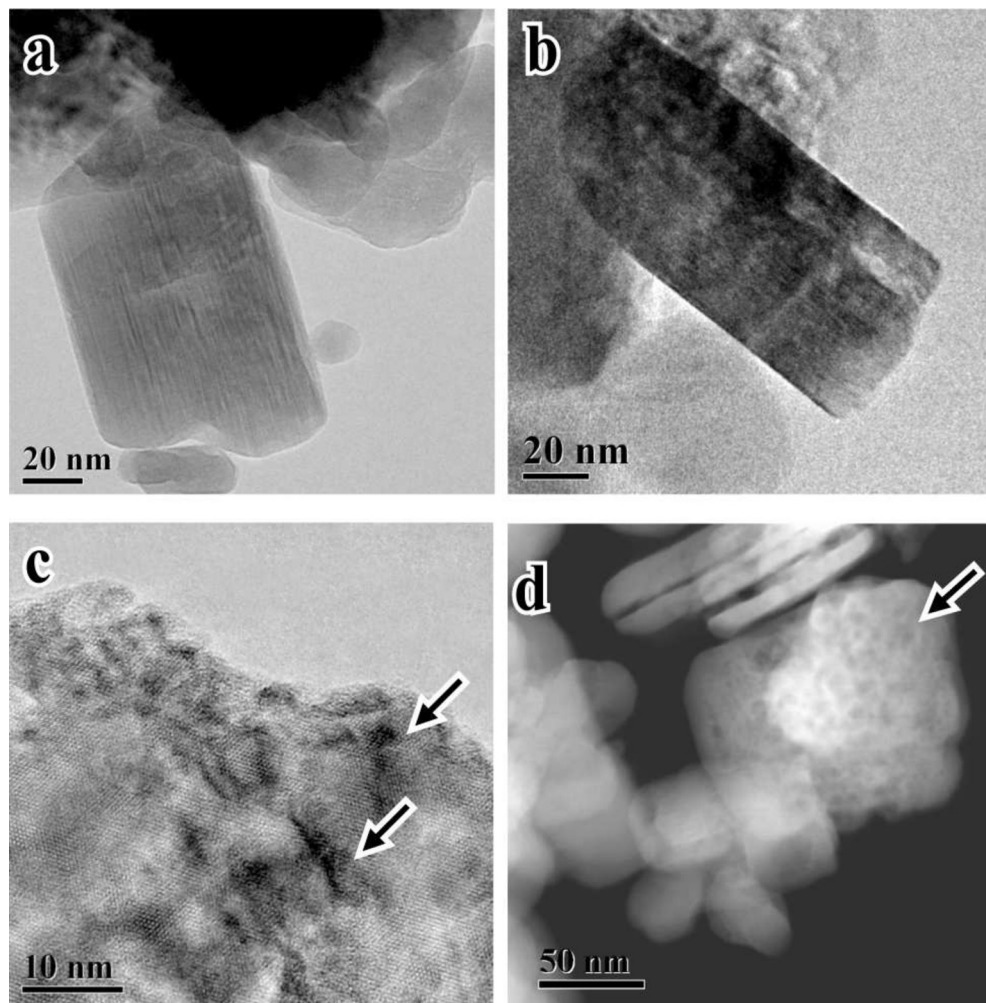


Fig. 3. TEM and ADF-STEM images of $\text{Li}_{1+x}(\text{Ti}_{0.4}\text{Mn}_{0.6})_{1-x}\text{O}_2$ particles before and after the carbothermal reduction. TEM images before (a) and after (b) the reduction. Enlarged TEM (c) and ADF-STEM (d) images after the reduction.

size of primary particles is approximately 50–300 nm. Polygonal-shaped and well-faceted particles having flat surfaces are often observed in TEM as shown in Fig. 3a and b. The apparent difference before and after the reduction is not observed in these TEM images. The particles presenting complicated diffraction contrasts due to crystalline defects or surface defects are often observed in the sample after the reduction as shown in Fig. 3c. The contrast is caused by the porous structure of the particle as examined by the ADF-STEM image in Fig. 3d. The irregular contrast is observed at the particle with porous structure as indicated by an arrow, while the particles in the left-hand side show uniform contrast. Note that the value of the BET surface area is changed from 18.0 to 24.4 m² g⁻¹

before and after the reduction. The porous particle is often observed in the sample after the reduction, while such particles are not observed in the sample before the reduction. Similar structure was observed in Fe-substituted Li₂MnO₃ particles after charge and discharge [9]. EELS analyses also revealed that the structure change is caused by extraction of oxygen from Fe-substituted Li₂MnO₃ particles during charging process [10]. Thus similar phenomenon is expected in the present Li_{1+x}(Ti_{0.4}Mn_{0.6})_{1-x}O₂ particles.

Fig. 4 indicates the high-magnification ADF-STEM images of Li_{1+x}(Ti_{0.4}Mn_{0.6})_{1-x}O₂ before (Fig. 4a and b) and after the carbo-thermal reduction (Fig. 4c and d) taken along the [010], and [110] or [100] zone axes (monoclinic, C2/m). The schematic drawings of the

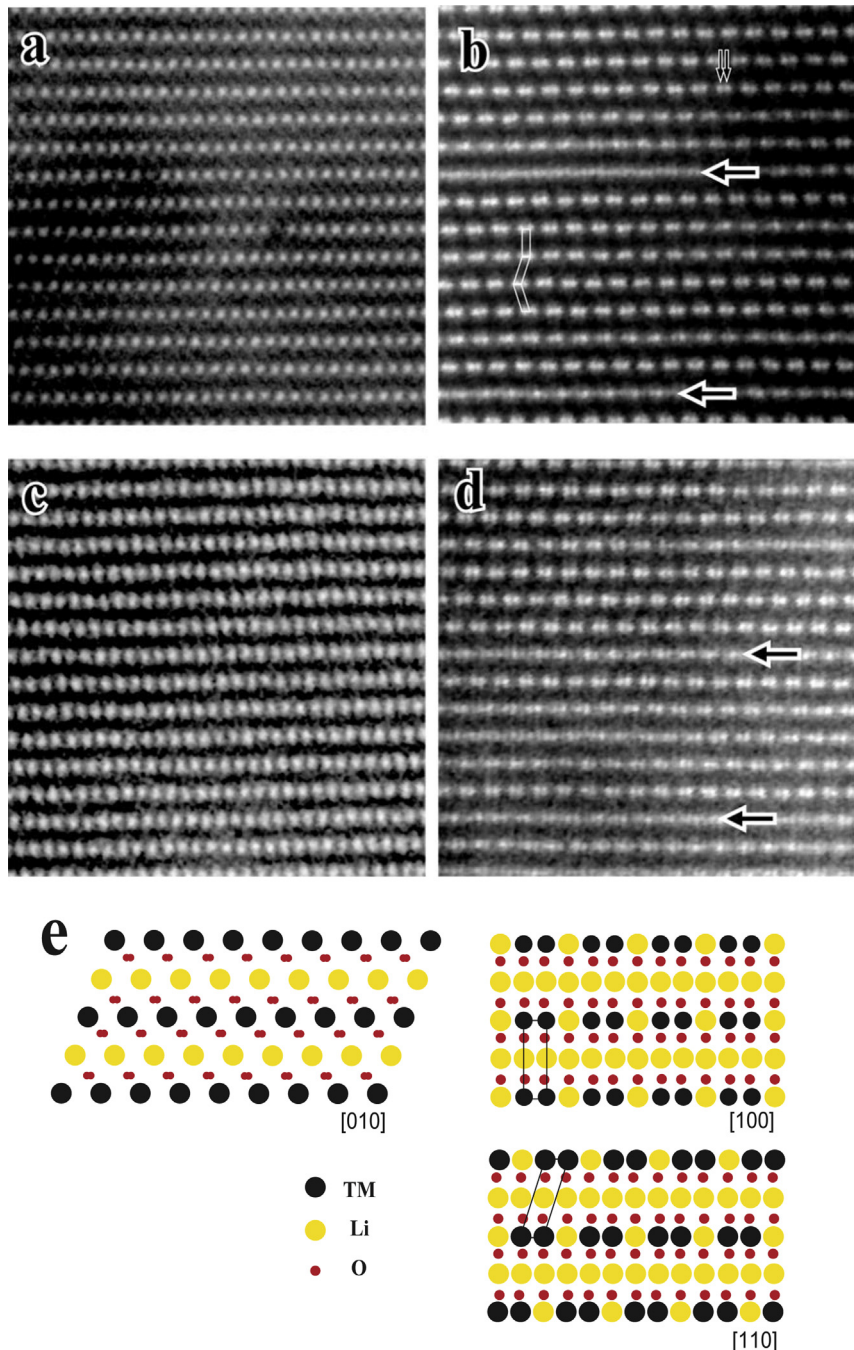


Fig. 4. High-resolution ADF-STEM images of Li_{1+x}(Ti_{0.4}Mn_{0.6})_{1-x}O₂ particles before and after the carbo-thermal reduction. (a) [010] and (b) [100] or [110] zone axis, before the reduction, (c) [010] and (d) [100] or [110] zone axis, after the reduction, and (e) schematic drawings of the projected crystal structures along [010], [100] or [110] zone axis.

crystal structure along the [010], [110] and [100] axes are also indicated in Fig. 4e. Fig. 4b and d was obtained from the areas where the value of $Ti/(Ti + Mn)$ was $44 \pm 2.0\%$ and $43 \pm 4.8\%$, respectively. These values are near to the average in $Li_{1+x}(-Ti_{0.4}Mn_{0.6})_{1-x}O_2$. The bright spots in the ADF-STEM images directly correspond to the atomic columns of transition-metal atoms, and oxygen and lithium columns are not detected in these ADF-STEM images. The ADF-STEM images in Fig. 4b and d indicate the close-packed lattice ordering Li and transition metal structure in two dimensional $\sqrt{3} \times \sqrt{3}$ structure as shown in previous reports [11–15]. Similar structure also observed in our samples. The disordered transition-metal ion distribution of closed packing lattice and stacking faults are also observed directly in the ADF-STEM image as indicated by large arrows in Fig. 4b and d. Fluctuation of ordered structure is also observed in the image. Although stacking faults can be interpreted as the partially formed C2/c structure, it is difficult to distinguish two crystalline structures in such a local region. The pair of two bright contrasts indicated by small arrows is the transition metal atomic columns, and the dark regions between the transition metal pairs correspond to the Li atomic columns (2b site) in the closed-packed layer. Although the bright contrast is not seen at the dark region when the complete ordered structure is formed in the closed-packed layer, the bright contrast often

appears in some atomic layer as indicated by a large arrow. This means that Li sites (2b site) in the closed-packing layer are occupied by transition metals. The significant differences are not observed in basic crystalline structure in atomic scale. Although the disordered structure is notable in Fig. 4d as indicated by arrows, the conclusion whether the lattice defects are increased after the reduction treatment should be derived after the statistical analysis of many images, because the ADF-STEM images are just recorded at limited local regions. The apparent displacement of transition-metal atoms to Li sites (2c or 4h site) is not observed in the HAADF-STEM image which was observed in the $Li[Ni_{0.17}Li_{0.2}Co_{0.07}Mn_{0.56}]O_2$ sample after charge [13]. Because a small amount of transition-metal atoms seems to be moved to the lithium layers, it was not detected in ADF-STEM for the $Li_{1+x}(Ti_{0.4}Mn_{0.6})_{1-x}O_2$ particle after the reduction, while the XRD analyses indicate that the amount of transition-metal atoms moved to Li layers is increasing after the reduction.

3.2. Distribution of Ti and Mn

EELS measurements were carried out for both the samples. Residual carbons originated from sucrose are occasionally observed on the surface of $Li_{1+x}(Ti_{0.4}Mn_{0.6})_{1-x}O_2$ particles after the reduction. Fig. 5 shows the results of EELS measurement of

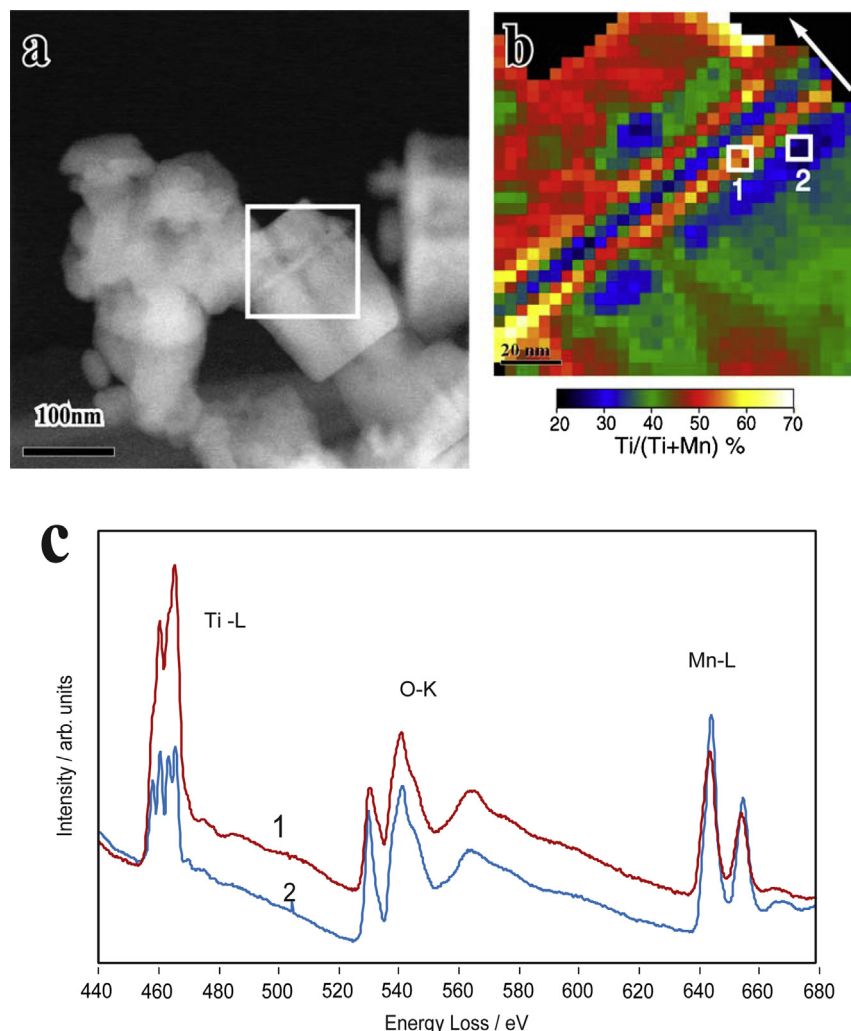


Fig. 5. Elemental mapping and EELS spectra of a $Li_{1+x}(Ti_{0.4}Mn_{0.6})_{1-x}O_2$ particle before the reduction. (a) ADF-STEM image, (b) transition-metal distribution mapping, and (c) EELS spectra from the white rectangle areas 1 and 2 in (b).

$\text{Li}_{1+x}(\text{Ti}_{0.4}\text{Mn}_{0.6})_{1-x}\text{O}_2$ before the reduction. The EELS spectra were measured with the 0.25 eV energy dispersion in order to obtain Ti *L* edge, O *K* edge and Mn *L* edge in 2048 CCD channel. Fig. 5b shows the transition-metal distribution by the STEM-EELS spectrum imaging method [16,17] for the area indicated by a white rectangle in the ADF-STEM image of Fig. 5a. The elemental mapping of the relative transition-metal concentration, $\text{Ti}/(\text{Ti} + \text{Mn})$ value, shows that Ti and Mn are not uniformly distributed in nano-scale within a primary particle, which is quite similar to Fe-substituted Li_2MnO_3 [16]. Fig. 5c shows corresponding EELS spectra from the white squares 1 and 2 in Fig. 5b, where the ratio of the intensities of Ti *L*-edge and Mn *L*-edge peaks is quite different for the two sites.

Moreover, it is also revealed that the distribution of each transition-metal concentration is not random or isotropic in a primary particle. The anisotropy of transition-metal distribution is observed in Fig. 5b. The distribution is suddenly changed along a specific direction as indicated by an arrow in Fig. 5b. The direction is [103], (monoclinic, $C2/m$) which was confirmed by an atomically-resolved high-resolution ADF-STEM image of this particle. This direction is almost perpendicular to the (001) plane as the closed-packed plane in the monoclinic Li_2MnO_3 crystal. The present result implies that the interaction between the close-packing layers is relatively weak and the fluctuation of the composition easily occurs on the (001)-plane stacking direction. Note that the (001) atomic plane or (001) surface has special characters as frequent observations of (001) stacking faults and large (001) surface facets in

primary particles. The space group of pure Li_2MnO_3 and Li_2TiO_3 is $C2/m$ and $C2/c$ respectively, and the lattice constants and ionic radius of Mn^{4+} (0.530 Å) and Ti^{4+} (0.605 Å) are also greatly different from each other. Therefore, it is hard to form the complete solid solution between Li_2MnO_3 and Li_2TiO_3 , resulting in the compositional fluctuation, associated with (001) stacking faults nearly perpendicular to the [103] direction.

Fig. 6 shows the results of EELS measurement of $\text{Li}_{1+x}(\text{Ti}_{0.4}\text{Mn}_{0.6})_{1-x}\text{O}_2$ after the reduction. Fig. 6b shows the transition-metal distribution by the STEM-EELS spectrum imaging method for the area indicated by a white rectangle in the ADF-STEM image of Fig. 6a. The feature of the distribution is basically similar to that before the reduction process in Fig. 5b. The distribution of transition metals suddenly changes along the [103] direction, similarly. This indicates that drastic changes in the transition-metal distribution do not occur by the reduction treatment.

3.3. Valence states of Ti and Mn

The valence state of transition-metal atoms is important for the electrochemical properties of positive electrode materials for extraction and insertion of Li ions. The EELS measurement with high energy resolution for the Ti and Mn *L*-edge energy-loss near-edge structure (ELNES) was applied to particles before and after the reduction, and those with uniform contrast and with irregular contrast, respectively. Fig. 7 shows Ti *L*-edge ELNES obtained from

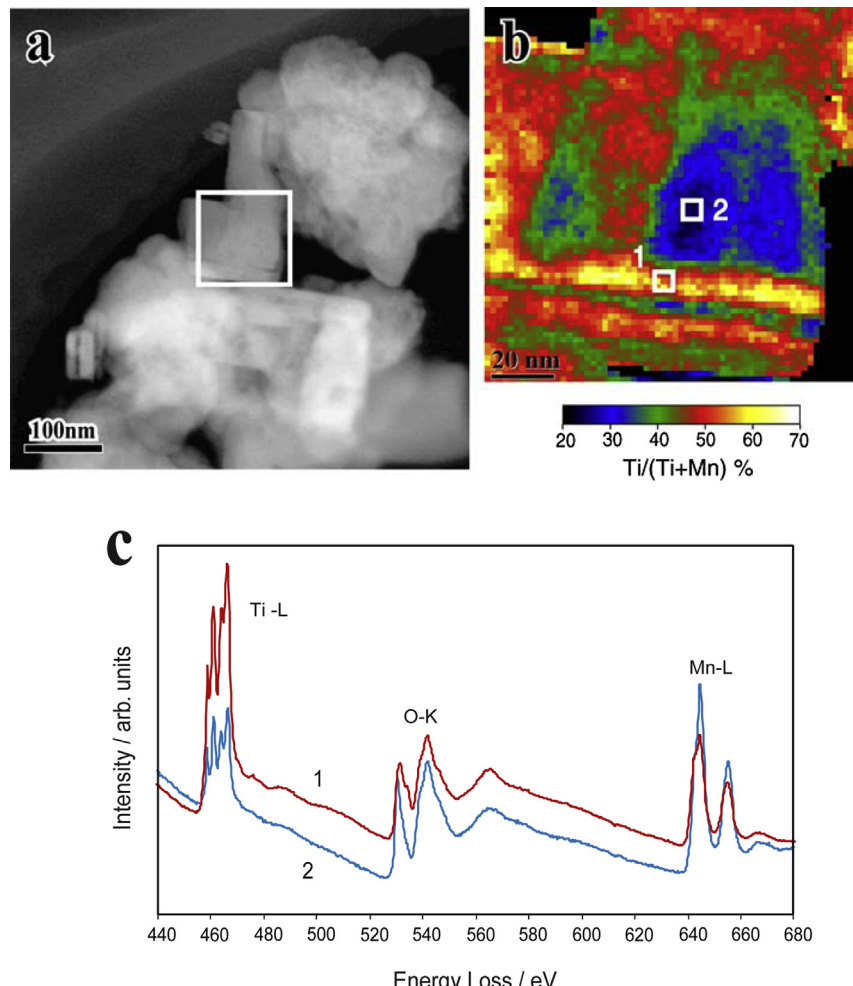


Fig. 6. Elemental mapping and EELS spectra of a $\text{Li}_{1+x}(\text{Ti}_{0.4}\text{Mn}_{0.6})_{1-x}\text{O}_2$ particle after the carbothermal reduction. (a) ADF-STEM image, (b) transition-metal distribution mapping, and (c) EELS spectra from the white rectangle areas 1 and 2 in (b).

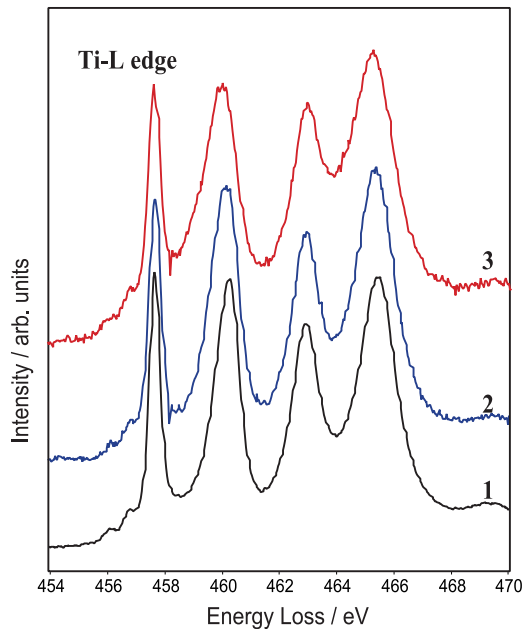


Fig. 7. Ti *L*-edge EELS spectra obtained from $\text{Li}_{1+x}(\text{Ti}_{0.4}\text{Mn}_{0.6})_{1-x}\text{O}_2$ particles before (spectrum 1) and after the reduction (spectra 2 and 3). Spectra 2 and 3 were obtained from the particles with uniform and irregular contrasts in the ADF-STEM image, respectively.

the particle before the reduction (spectrum 1) and from the particles after the reduction with uniform contrast (spectrum 2) and irregular contrast (spectrum 3). The Ti *L* edge is mainly reflecting the electron transition from Ti-2p to Ti-3d unoccupied states. The sharp four peaks caused by the spin orbit interaction and crystal field [18] are observed clearly due to the high energy resolution by monochromator. The characteristic four peaks are usually observed for the Ti^{4+} surrounded by six oxygen atoms with octahedral coordination, such as rutile and anatase TiO_2 . There is no significant difference in these Ti *L*-edge ELNES and it can be concluded that most Ti atoms remain as Ti^{4+} even after the reduction treatment. This result is consistent with the result by X-ray absorption near-edge structure (XANES) measurement reported before [6]. Regardless of the local compositional variations of the transition metals, Ti atoms were Ti^{4+} in all measured areas.

Fig. 8 shows the ADF-STEM image of $\text{Li}_{1+x}(\text{Ti}_{0.4}\text{Mn}_{0.6})_{1-x}\text{O}_2$ particles after the reduction and the Mn *L*-edge EELS spectra obtained from the sample before and after the reduction. The spectra 1 and 2 in Fig. 8b were derived from white rectangle areas 1 and 2 indicated in the ADF-STEM image in Fig. 8a. In the ADF-STEM image, the contrast is not uniform in the central particle due to porous structure, while the particles in both sides present uniform contrast. The fine structure of spectrum 2 from the porous particle is apparently different from the spectrum 1 of the particle with uniform contrast. It was confirmed that the energy drift during measurement is negligible in this experiment. The ELNES of spectrum 1 is the same as the spectrum obtained from the sample before the reduction, expressed by a red line in Fig. 8b, in which the Mn atoms are Mn^{4+} [19] as reported by chemical analysis. The peak positions and the shape of the spectrum 2 are apparently different from the spectrum 1. The high energy resolution EELS with monochromator revealed the fine structure of EELS spectra clearly. The characteristic peak of Mn^{4+} at 641 eV could be clearly identified which was appearing as shoulder of the large peak at 643 eV by conventional EELS with the energy resolution of about 1 eV. The EELS spectrum indicates that the reduced Mn atoms exist at the

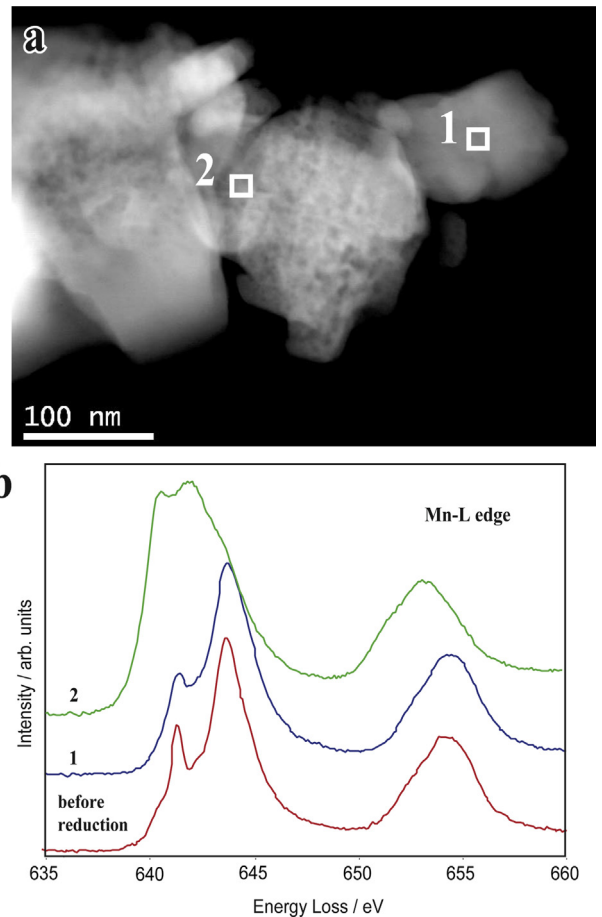


Fig. 8. ADF-STEM image of $\text{Li}_{1+x}(\text{Ti}_{0.4}\text{Mn}_{0.6})_{1-x}\text{O}_2$ particles after the reduction, and Mn *L*-edge EELS spectra before and after the reduction. (a) ADF-STEM image, (b) Mn *L*-edge EELS spectra from the particle before the reduction (red line) and the particles after the reduction with uniform contrast (spectrum 1) and porous structure (spectrum 2). (For interpretation of the references to color in this figure legend, the reader is referred to the web version of this article.)

corresponding area. Although the strong electron beam irradiation often causes the reduction of transition metal oxide, such effect was carefully reduced in this experimental condition.

The XANES spectra revealed that reduced Mn ions are slightly generated by the reduction treatment in our previous report [6]. Although it is difficult to compare the amount of reduced Mn atoms quantitatively between the results by STEM-EELS and XANES, the present STEM-EELS result does not contradict the XANES result. It is important to elucidate the location of reduced phases in nano-scale by electron microscopy, which could not be clarified by XANES. The valence state of Mn was estimated by the intensity ratio of Mn L_2 and L_3 edges in our previous report [16], but in present experiment, the valence state of Mn is apparently identified in ELNES due to the high energy resolution as indicated in Fig. 8b. Therefore the MLLS fitting method can be applied to the mapping of the valence state of Mn. Fig. 9 shows the ADF-STEM image and the corresponding quasi valence-state map of Mn atoms in the sample obtained from the spectra 1 and 2 indicated in Fig. 8b. In Fig. 9b and c, the coefficient value of each component of spectra 1 and 2 is mapped two-dimensionally. The distribution of reduced Mn atoms (component 2) is dominantly observed in the central particle with porous structures, while the particles in the both sides are mainly composed of Mn^{4+} component (component of spectrum 1). The Mn^{4+} components also exist in the central particle, suggesting that

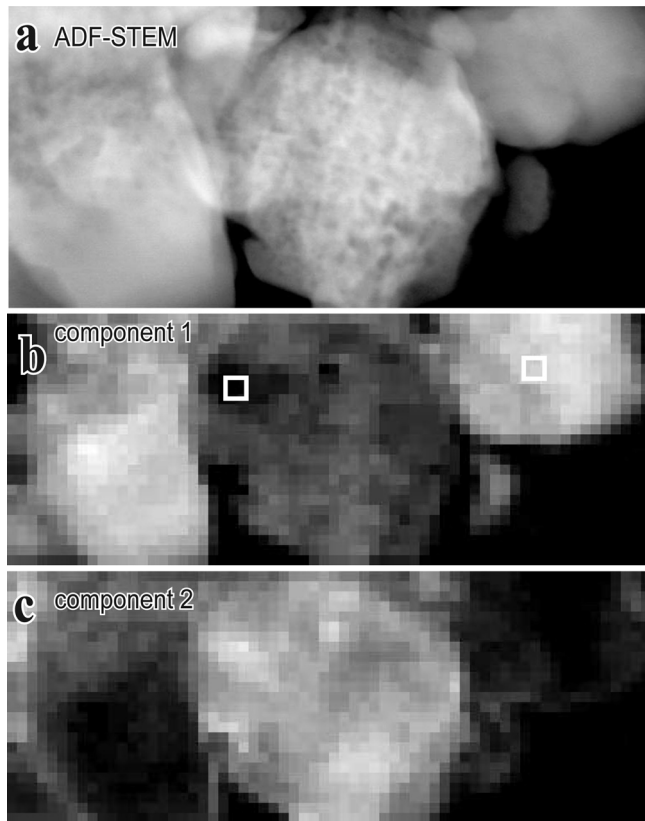


Fig. 9. Valence-state distribution image of $\text{Li}_{1+x}(\text{Ti}_{0.4}\text{Mn}_{0.6})_{1-x}\text{O}_2$ particles by the MLLS fitting. (a) ADF-STEM image, (b) distribution of component 1 (spectrum 1 in Fig. 8b), and (c) distribution of component 2 (spectrum 2 in Fig. 8b).

the particle contains both Mn^{3+} and Mn^{4+} . The Mn atoms may easily release the oxygen atoms comparing to the Ti atoms. These results indicate that Mn atoms are selectively reduced by the carbothermal reduction treatment, accompanied by the morphology change of a primary particle. The reduced Mn ions can contribute to the capacity in the initial charge process by the oxidation from Mn^{3+} to Mn^{4+} . In previous reports [20,21], it is indicated that the reduced Mn in Li_2MnO_3 or $\text{Li}_2\text{MnO}_3\text{--LiMO}_2$ improve the electrochemical properties. The spatial distribution of reduced Mn ions was revealed by the STEM-EELS method in the present experiments with nano-scale. Present STEM-EELS experiments revealed that the reduced Mn ions are not uniformly distributed in a whole sample, where some particles contain high density of reduced Mn ions, and others are mainly composed of Mn^{4+} . Although the reason is not clear, the effects of the reduction process seem to occur inhomogeneously, depending on the local structure or composition. The relation between the distribution of reduced Mn and the transition-metal compositional variation was not identified in the present experiment. There may be a possibility that Mn atoms in Mn-rich regions are reduced preferentially because Ti atoms are never reduced by the reduction treatment, while we have no apparent evidence for the relation between the transition-metal distribution and the reduction area of Mn.

The present results indicate that there is a possibility for the further improvement of electrochemical performance of this material by attaining optimized microstructures or local compositions via the optimized processes of formation and pre-reduction. If the compositional distribution of transition metals becomes uniform, the formation of manganese-based impurity phases such as LiMnO_2 and/or MnO seem to be prevented, unless the high-

temperature reduction processes, which may enable us to produce a high quality sample with much higher Mn content (Ti content less than 30%) without forming impurity phases. As recently examined [22], in the case of Fe and Ni substituted Li_2MnO_3 , more uniform distribution of transition-metal components surely leads to better electrochemical performance. Of course, in addition to the uniform compositional distribution, the uniform quality or sizes of particles may be also important to attain uniform reduction. In any case, it is crucial to perform the present type of electron microscopy observation, closely combined with the process optimization and the examination of electrochemical performance, which should provide reliable relation among the process conditions, microstructures and electrochemical performance in the near future.

4. Conclusion

The following conclusions have been drawn through the application of aberration-corrected analytical TEM and EELS with monochromator to 40% Ti-substituted Li_2MnO_3 positive electrode material before and after the carbothermal reduction.

- 1) The distribution of Mn and Ti was clarified by the STEM-EELS spectrum imaging method, which reveals nano-scale inhomogeneous distribution of the two species inside each primary particle.
- 2) Reduced Mn ions were partially identified in the sample after the carbothermal reduction, while Ti ions remain as Ti^{4+} .
- 3) The inhomogeneous distribution of reduced Mn ions among primary particles was revealed via the STEM-EELS method with higher energy resolution by the monochromator.
- 4) The reduction of Mn is accompanied by the morphology change of primary particles as porous structures.

Acknowledgment

This study was supported financially by a national project (Li-EAD project) of the Ministry of Economy, Trade and Industry (METI) and the New Energy and Industrial Technology Development Organization (NEDO).

References

- [1] K. Numata, C. Sakai, S. Yamanaka, *Chem. Lett.* (1997) 725–726.
- [2] Z. Lu, L.Y. Beaulieu, R.A. Donaberger, C.L. Thomas, J.R. Dahn, *J. Electrochem. Soc.* 149 (2002) A778–A791.
- [3] M.M. Thackeray, S. Kang, C.S. Johnson, J.T. Vaughey, R. Benedek, S.A. Hackney, *J. Mater. Chem.* 17 (2007) 3112–3115.
- [4] C.S. Johnson, N. Li, C. Lefief, J.T. Vaughey, M.M. Thackeray, *Chem. Mater.* 20 (2008) 6095–6106.
- [5] M. Tabuchi, A. Nakashima, K. Ado, H. Kageyama, K. Tatsumi, *Chem. Mater.* 17 (2005) 4668–4677.
- [6] M. Tabuchi, Y. Nabeshima, T. Takeuchi, H. Kageyama, J. Imaizumi, H. Shibuya, J. Akimoto, *J. Power Sources* 221 (2013) 427–434.
- [7] F. Izumi, T. Ikeda, *Mater. Sci. Forum* 321–324 (2000) 198–203.
- [8] A. Maigné, R.D. Twisten, *J. Electron Microsc.* 58 (2009) 99–109.
- [9] J. Kikkawa, T. Akita, M. Tabuchi, M. Shikano, K. Tatsumi, M. Kohyama, *J. Electrochem. Soc.* 156 (2009) A839–A845.
- [10] J. Kikkawa, T. Akita, M. Tabuchi, K. Tatsumi, M. Kohyama, *J. Electrochem. Soc.* 158 (6) (2011) A760–A768.
- [11] C.H. Lei, J. Bareño, J.G. Wen, I. Petrov, S.-H. Kang, D.P. Abraham, *J. Power Sources* 178 (2008) 422–433.
- [12] J.G. Wen, J. Bareño, C.H. Lei, S.H. Kang, M. Balasubramanian, I. Petrov, D.P. Abraham, *Solid State Ionics* 182 (2011) 98–107.
- [13] A. Ito, K. Shoda, Y. Sato, M. Hatano, H. Horie, Y. Ohsawa, *J. Power Sources* 196 (2011) 4785–4790.
- [14] K.A. Jarvis, Z. Deng, L.F. Allard, A. Manthiram, P.J. Ferreira, *Chem. Mater.* 23 (2011) 3614–3621.
- [15] A. Boulineau, L. Simonin, J.-F. Colin, E. Canévet, L. Daniel, S. Patoux, *Chem. Mater.* 24 (2012) 3558–3566.

- [16] J. Kikkawa, T. Akita, M. Tabuchi, M. Shikano, K. Tatsumi, M. Kohyama, *Appl. Phys. Lett.* 91 (2007) 054103.
- [17] J. Kikkawa, T. Akita, M. Tabuchi, M. Shikano, K. Tatsumi, M. Kohyama, *Electrochem. Solid-State Lett.* 11 (2008) A183–A186.
- [18] R. Brydson, H. Sauer, W. Engel, J.M. Thomas, E. Zeitler, N. Kosugi, H. Kuroda, *J. Phys. Condens. Matter* 1 (1989) 797–812.
- [19] B. Ammundsen, J. Paulsen, *Adv. Mater.* 13 (2001) 943–956.
- [20] K. Kubota, T. Kaneko, M. Hirayama, M. Yonemura, Y. Imanari, K. Nakane, R. Kanno, *J. Power Sources* 216 (2012) 249–255.
- [21] A. Abouimrane, O.C. Compton, H. Deng, I. Belharouak, D.A. Dikin, S.T. Nguyen, K. Amine, *Electrochem. Solid-State Lett.* 14 (2011) A126–A129.
- [22] M. Tabuchi, Y. Nabeshima, T. Takeuchi, H. Kageyama, K. Tatsumi, K. Tanimoto, J. Akimoto, H. Shibuya, J. Imaizumi, in: *Abstracts of the 52nd Battery Symposium in Japan*, Tokyo, 2011, 3A01.